POLITECNICO DI TORINO
Repository ISTITUZIONALE

A New Model-Based Approach for the Development of Freeze-Drying Cycles Using a Small-Scale Freeze-Dryer

Original
A New Model-Based Approach for the Development of Freeze-Drying Cycles Using a Small-Scale Freeze-Dryer / Massei, A., Fissore, D.. - In: JOURNAL OF PHARMACEUTICAL SCIENCES. - ISSN 1520-6017. - STAMPA. - 112:8(2023), pp. 2176-2189. [10.1016/j.xphs.2023.05.007]

Availability:
This version is available at: 11583/2982847 since: 2023-10-08T17:16:29Z

Publisher:
elsevier

Published
DOI:10.1016/j.xphs.2023.05.007

Terms of use:

This article is made available under terms and conditions as specified in the corresponding bibliographic description in the repository

Publisher copyright
Elsevier postprint/Author's Accepted Manuscript

© 2023. This manuscript version is made available under the CC-BY-NC-ND 4.0 license
http://creativecommons.org/licenses/by-nc-nd/4.0/.The final authenticated version is available online at:
http://dx.doi.org/10.1016/j.xphs.2023.05.007

(Article begins on next page)

25 November 2026

Applied Materials Today 49 (2026) 103155

Contents lists available at ScienceDirect

Applied Materials Today

journal homepage: www.elsevier.com/locate/apmt

Exploring functionalized nanocrystalline cellulose binders for potassium-ion batteries

Sofia Raviolo [a,†], Rosarita D'Orsi [b,†], Sabrina Trano [a], Laura Spagnuolo [b], Matteo Cei [b], Alessandra Operamolla [b,*], Federico Bella [a,*]

[a] Dipartimento di Scienza Applicata e Tecnologia, Politecnico di Torino, Corso Duca degli Abruzzi 24, Torino 10129 Italy
[b] Dipartimento di Chimica e Chimica Industriale, Università di Pisa, Via Giuseppe Moruzzi 13, Pisa 56124 Italy

ARTICLE INFO

Keywords:
Cellulose nanocrystals
Binder
Potassium-ion battery
Gel

ABSTRACT

The development of sustainable and efficient binder materials is crucial to improve the performance and environmental compatibility of potassium-ion batteries (KIBs). In this study, we investigate the use of cellulose nanocrystals (CNCs) as eco-friendly binders for carbon-based anodes for KIBs. Three types of CNCs are synthesized from microcrystalline cellulose via enzymatic, hydrochloric acid, and sulfuric acid hydrolysis, and fully characterized by spectroscopic, elemental, crystallographic, and morphological analyses. Their electrochemical stability is confirmed by cyclic voltammetry on binder-only electrodes, which shows negligible activity in the 0.01–3 V vs. K^+/K window. When incorporated as binders into anode electrodes based on commercial Super C45 carbon, CNCs enable excellent electrochemical performance, outperforming conventional carboxymethyl cellulose-based counterparts. Among them, CNCs synthesized from enzymatic hydrolysis provide the best results in terms of specific capacity, capacity retention (97 % after 100 cycles), rate capability, and electrode morphology. These improvements are attributed to the neutral surface chemistry and enhanced structural homogeneity. Our findings highlight CNCs as promising, low-cost, and sustainable binder materials for next-generation KIB systems.

1. Introduction

It is well known that Li-ion batteries (LIBs) have taken the lead as portable energy storage devices over the past few decades [1]. However, in many applications – particularly in large-scale energy storage systems where high energy density is not the primary requirement – alternative technologies that are more sustainable and cost-effective are being actively explored [2–11]. In this context, potassium-ion batteries (KIBs) have gained considerable attention due to several advantages that make them competitive with LIBs [12]. One key benefit of implementing potassium in batteries is its abundance in the Earth crust (2.09 wt % for K vs 0.0017 wt % for Li) and its homogeneous global distribution, making it a significantly cheaper and more accessible resource [13]. Additionally, potassium exhibits a low standard reduction potential (−2.93 V vs. standard hydrogen electrode), which is the closest to lithium one (−3.04 V) [14]. Furthermore, the weak Lewis acidity of potassium results in smaller sizes of solvated ions, enhancing their diffusion rate and facilitating ionic transport across the electrode/electrolyte interface [15,16]. Despite these advantages, the larger size of desolvated potassium ions (d_{K^+} = 1.38 Å) compared to lithium counterpart (d_{Li^+} = 0.76 Å) represents a critical challenge [12]. The substantial volume changes associated with the potassiation/depotassiation processes can lead to mechanical stress, electrode cracking, and, ultimately, rapid capacity fading [17].

To address these issues, the development of more effective binder materials has become increasingly important in enhancing the electrochemical performance and durability of KIB electrodes [18,19]. Binders play a key role in battery electrodes by holding together their different components without interfering with the electrochemical reactions occurring during the charge/discharge processes [20]. To achieve this, they must be electrochemically stable within the working potential window, elastic enough to tolerate the significant volume changes that particularly affect this type of system, and provide strong adhesion to the current collectors to facilitate the exchange of electric charge with

* Corresponding authors.
E-mail addresses: alessandra.operamolla@unipi.it (A. Operamolla), federico.bella@polito.it (F. Bella).
† These authors contributed equally to the work.

https://doi.org/10.1016/j.apmt.2026.103155
Received 31 October 2025; Received in revised form 14 January 2026; Accepted 15 February 2026
2352-9407/© 2026 The Authors. Published by Elsevier Ltd. This is an open access article under the CC BY license (http://creativecommons.org/licenses/by/4.0/).

the external circuit [21]. Currently, one of the most widely used binders in this area is poly(vinylidene fluoride) (PVDF), which meets many of these criteria and has been the binder of choice in most commercial battery systems. However, PVDF presents several drawbacks. Most notably, its processing requires the use of *N*-methyl-2-pyrrolidone, a toxic and costly organic solvent. Other disadvantages include its high production costs and challenges related to recyclability and environmental impact [21]. That is why different alternatives are being studied to replace PVDF for more sustainable and inexpensive materials [22].

In this scenario, cellulosic materials can be considered promising, safe, and sustainable alternatives to traditional binders, thanks to their abundance, thermal stability, good mechanical properties, hydrophilic character, and, not least, their economic convenience [23,24]. This hydrophilic biopolymer is essential in the structure of plant cell walls and is also present in fungi, invertebrates, and some marine creatures, among others [25]. As a consequence, cellulose is an abundant material that can be obtained from renewable resources and, thus, it is biodegradable and safe for human health. Cellulose nanocrystals (CNCs) represent the crystalline regions within cellulose fibrils and can be produced by applying chemical processes to isolate these crystalline domains by a top-down approach. They typically display a diameter in the range between 5 and 50 nm and a length ranging from 100 to 500 nm [26]. Nanostructured cellulose, indeed, could ensure a better mobility of ions thanks to the high specific surface area with respect to other forms of cellulose. Diverse kinds of hydrolytic reactions produce nanocrystals with different surface or crystalline properties: hydrochloric acid hydrolysis yields neutral nanocrystals (N—CNC), composed of pure cellulose, the surface of which is constituted by free hydroxyl groups [27]; sulfuric acid hydrolysis produces functionalized nanocrystals, in which primary hydroxyl groups are randomly sulfated (S-CNC) [28]. Given the toxicity and hazardousness of acids, the milder enzymatic hydrolysis with endoglucanases represents an effective alternative to prepare neutral nanocrystals (eN—CNC), avoiding the release of concentrated acid as a waste [29]. CNCs have been a popular choice for functional materials applications in a variety of fields – including biomedical applications [30], paper manufacture [31], and energy storage devices [32] – due to their flexibility, low density, and exceptional rheological properties [33]. These properties are largely attributed to the hydrogen-bonded crystalline network formed by primary and secondary hydroxyl groups on their surfaces [34]. These groups not only promote structural organization through electrostatic interactions, but also offer chemical versatility, enabling functional modifications to tailor CNCs properties [35].

Despite the promising features of CNCs, their potential as binder materials in emerging battery systems – such as KIBs – remains largely unexplored. In this work, we synthesize and characterize three types of CNCs produced via different hydrolytic methods, and evaluate their performance as binders in carbon-based anodes for KIBs through various electrochemical techniques. A key aspect influencing their behavior is their dispersibility in polar solvents, which varies depending on their surface chemistry. S-CNC are more easily dispersed in polar solvents due to the surface charge repulsion of negative charges formed at pH > 1. In contrast, neutral CNCs (N—CNC and eN—CNC), lacking surface charges, tend to aggregate in aqueous suspension, which limits their widespread use and commercial availability [36]. To overcome this limitation, dimethyl sulfoxide (DMSO) was selected as an effective dispersing medium for all CNCs types. Thanks to its hydrogen bond-accepting nature, DMSO facilitates the separation of individual nanocrystals and promotes the formation of stable gels, even in the case of neutral CNCs. Finally, to contextualize our findings, we compare the electrochemical behavior of CNCs-based electrodes with those fabricated using commercial carboxymethyl cellulose (CMC), one of the most widely used cellulose-derived binders.

2. Experimentation

2.1. Materials and synthesis

Avicel PH-101 was purchased from Sigma-Aldrich and was used as the starting material for nanocrystalline cellulose isolation. Dialysis was carried out at room temperature against deionized water in nitrocellulose tubes with a cut-off of 12,400 Da. Hydrochloric acid (HCl), sulfuric acid (H_2SO_4), and DMSO were purchased from Sigma-Aldrich. Di-sodium hydrogen phosphate dihydrate ($Na_2HPO_4{\cdot}2H_2O$) and sodium phosphate monobasic dihydrate ($NaH_2PO_4{\cdot}2H_2O$) were purchased from Fluka. Endoglucanase from *Aspergillus niger* (1,4-(1,3:1,4)-β-D-glucan 4-glucan-hydrolase, EC3.2.1.2) was purchased from MP Biomedicals. Super C45 carbon black was purchased from Imerys, Timcal. CMC 2200, potassium bis(fluorosulfonyl)imide (KFSI), ethylene carbonate (EC), and diethyl carbonate (DEC) were purchased from DAICEL, BLDpharm and Merck, respectively.

2.1.1. N—CNC

To synthesize the neutral nanocrystals, 75 mL of deionized water were introduced in a 250 mL three-necked round-bottomed flask equipped with a water condenser and a mechanical stirrer. Then, the flask was cooled in an ice bath and 75 mL of concentrated HCl was added. After that, 7.50 g of Avicel PH-101 were added and the suspension was warmed to 105 °C for 6 h. The system was cooled to room temperature and diluted with 75 mL of distilled water and the mixture was transferred to polypropylene centrifugation tubes. Centrifugation at 4000 rpm was repeated four times, replacing the supernatant liquid with fresh deionized water until the pH was approximately 3. The cellulose residue was dialyzed against distilled water until neutrality using a cellulose nitrate membrane with a molecular weight cut-off of 12,400 Da. The suspension was sonicated with the aid of a Dr. Hielscher sonicator equipped with an ultrasonic horn with a 3.5 mm diameter (microtip) operated in pulsed mode, with a power of 40 W and 0.6 s pulses for 10 min. The resulting suspension was transferred to polypropylene centrifugation tubes and centrifuged at 1000 rpm for 10 min. The supernatant suspension was lyophilized, yielding 1.54 g of CNCs (21 % yield).

2.1.2. eN—CNC

Avicel pretreatment required the use of a ball mill with horizontal oscillation (BM500, Anton Paar) equipped with two 50 mL stainless steel jars and one 2.5 cm diameter ball for each jar. Each jar was loaded with 5 g of Avicel. The pretreatment was performed with a frequency of 3 Hz for 50 min without breaks. 5.04 g of ball-milled Avicel were added to 50 mL of 50 mM phosphate buffer (pH = 5.0) and homogenized with a tissue master. Then, *Aspergillus niger* endoglucanase (enzyme:cellulose = 1:10 ratio) was introduced into the suspension. The reaction mixture was shaken in an orbital shaker at 55 °C for 96 h at 150 rpm. After the incubation period, the reaction was transferred to a beaker and heated from 55 °C to 95 °C for 15 min to inactivate the enzyme. The resulting mixture was subjected to centrifugation at 4000 rpm for 10 min. This was followed by a washing step with 20 mL of 0.1 M HCl, followed by another centrifugation cycle at 4000 rpm for 10 min. To remove the HCl, the solution was subjected to multiple centrifugations with deionized H_2O (20 mL) at 4000 rpm for 10 min, discarding the supernatant each time, until neutrality was confirmed with litmus paper. Once neutral pH was reached, the suspension was subjected to a 24 h dialysis using a cellulose nitrate membrane with a molecular weight cut-off of 12,400 Da. Next, the suspension was subjected for 10 min to sonication with a 400 W Dr. Hielscher sonicator with a power of 40 W and pulses of 0.6 s. A final centrifugation at 1000 rpm for 10 min was conducted, and the supernatant containing nanocrystals was collected and lyophilized. The material was isolated with 76 % yield.

2.1.3. S-CNC

In order to obtain the sulfated cellulose nanocrystals, 250 mL of deionized water were introduced in a 1 L cylindrical reactor equipped with a water condenser and a mechanical stirrer. Then, the flask was cooled in an ice bath, and 250 mL of concentrated H_2SO_4 were added. After that, 30 g of Avicel pH-101 were added, and the suspension was warmed to 45 °C for 80 min. The system was cooled to room temperature, diluted with deionized water (250 mL), and the mixture was finally transferred to polypropylene centrifugation tubes. Centrifugation at 4000 rpm was repeated, replacing the supernatant liquid with fresh deionized water until the pH was approximately 1. The cellulose residue was dialysised against distilled water until neutrality using a cellulose nitrate membrane with a molecular weight cut-off of 12,400 Da. Then, the suspension was sonicated with the aid of a Dr Hielsher tip sonicator equipped with an ultrasonic horn with a 3.5 mm diameter (micro-tip) operated in pulsed mode, with a power of 40 W and 0.6 s pulses for 10 min. The resulting suspension was transferred to polypropylene centrifugation tubes and centrifuged at 4000 rpm for 10 min. The supernatant suspension was lyophilized, yielding 4.63 g of CNCs (15 % yield).

2.2. Gel preparation

For each sample, 30 mg of CNCs were added to 5 mL of DMSO. The suspension was sonicated with a Dr Hielscher tip sonicator equipped with an ultrasonic horn with a 3.5 mm diameter tip (micro-tip) operated in pulsed mode, with a power of 20 W and 0.8 s pulses. The gelation process took about 15 min for each sample.

2.3. Materials characterizations

Elemental analyses were performed on an Elementar Vario Micro Cube analyzer. Carbon, hydrogen, nitrogen, and sulfur contents were determined. All analyses were carried out on 5 mg of dry samples to evidence changes in sulfur or nitrogen content. Oxygen content was calculated for all samples by difference. All determinations were done in duplicate.

Attenuated total reflectance-Fourier transform infrared (ATR-FTIR) spectra were collected on a Thermo Fischer Nicolet iS50 FTIR instrument interfaced with an ATR ITX accessory equipped with a diamond crystal (radiation penetration approximately 2 μm at 1000 cm^{-1}). The spectra were recorded at room temperature, in air, in the range between 4000 and 650 cm^{-1}, with a resolution of 4 cm^{-1}, 16 accumulated scans, and a DTGS as a detector. The spectra were elaborated using the software SPECTRA.

Field emission scanning electron microscopy (FESEM) analyses were carried out on a FEI FEG-Quanta 450 instrument. Cellulose nanocrystals were deposited on glass from a DMSO suspension at a concentration of 1 mg L^{-1}. For the deposition, 20 μL of the suspension were cast on a round microscopy glass with 12 mm diameter. After 2 min, the drop was wiped off with a piece of clean filter paper. The sample was left to dry on air and then stored in a desiccator until the moment of the analysis. Samples were coated with platinum (5 nm) before analysis. For scanning electron microscopy/energy dispersive X-rays spectroscopy (SEM-EDS) analyses, samples were drop cast on glass from a 1 mg mL^{-1} dispersion in water. A Bruker Quantax EBSD/EDS analysis system was used for phase identification and textural mapping. EDS provided information about element chemistry supporting NCHS elemental analyses.

High-resolution synchrotron X-rays diffraction (XRD) and total scattering measurements were performed at beamline ID31 at the European Synchrotron Radiation Facility (ESRF). The sample powders were loaded into cylindrical slots (approx. 1 mm thickness) held between Kapton windows in a high-throughput sample holder. Each sample was measured in transmission geometry with an incident X-rays energy of 75.051 keV (λ = 0.16520 Å). Measured intensities were collected using a Pilatus CdTe 2 M detector (1679 × 1475 pixels, 172 × 172 μm^2 each) positioned with the incident beam in the corner of the detector. The sample-to-detector distance was approximately 1.5 m for the high-resolution measurements and 0.3 m for the total scattering measurements. Background measurements for the empty windows were measured and subtracted. NIST SRM 660b (LaB6) was used for geometry calibration performed with the software pyFAI followed by image integration including a flat-field, geometry, solid-angle, and polarization corrections. The 2θ axis was normalized with the respective wavelength to obtain an absolute axis on momentum transfer Q, where $Q = 4\pi \frac{\sin\theta}{\lambda}$.

2.4. Electrodes preparation and characterization

Electrochemical characterizations were performed in two different electrode configurations to assess both the binders alone (binder electrodes) and commercial Super C45 carbon combined with each binder (C45/binder electrodes). The choice of C45 as the active material in this work was guided by two main considerations: the need to investigate binder compatibility with amorphous carbon (the electrostatic and chemical features of which make the binding process more challenging) and its optimal compatibility with CMC, previously demonstrated in another study [37], which is used here as the reference binder for comparison. The binder electrodes were prepared by mixing each CNC material with DMSO at a concentration of 30 mg mL^{-1}. The resulting gels were coated onto aluminium foil using a doctor blade with a wet controlled thickness of 100 μm. The coated films were dried in an oven at 50 °C for 2 h and then punched into 10 mm disks. Additionally, bare aluminum foil was cut into disks, used as control electrodes for comparative analysis. All electrodes were subsequently dried under vacuum at 80 °C for 2 h in a Büchi oven.

Similarly, the C45/binder electrodes were prepared by mixing 80 wt % of Super C45 carbon and 20 wt % per each binder material, using DMSO as a solvent. The mixture was subjected to ball milling at 30 Hz for 20 min, and the resulting slurry was coated onto aluminium foil using a doctor blade at a wet thickness of 100 μm. After drying at 50 °C for 2 h, the electrodes were punched into 15 mm disks and subjected to vacuum drying at 120 °C for 4 h in a Büchi oven. The C45 areal loading of the obtained electrodes was 0.85 ± 0.07 mg cm^{-2}. For comparative analysis, additional electrodes were prepared using commercial CMC as the binder, following the same procedure, but employing deionized water as solvent.

Cell assembly was performed in an argon-filled glove box (MBRAUN MB10 compact, $O_2 < 0.5$ ppm, $H_2O < 0.5$ ppm) in two different configurations: a three-electrode T-cell was used to characterize the binder electrodes, while a half-cell configuration in LIR2032 coin cell was used to test the C45/binder electrodes. Metallic potassium was used as both the counter and reference electrode, Whatman glass fiber disks were used as separators, and a 1 M solution of KFSI in EC:DEC (1:1, v:v) was used as the electrolyte.

Galvanostatic cycling (GC) of the C45/binder electrodes were conducted using an Arbin LBT-21084C battery tester within a potential range of 0.01–3.00 V vs. K^+/K, at a constant current density of 0.05 A g^{-1} over 100 cycles. To evaluate rate performance, after 20 cycles at 0.05 A g^{-1}, the current density was successively increased to 0.1, 0.2, 0.4, 0.8, 1.0, and 2.5 A g^{-1}, with 10 cycles at each rate, followed by 20 final cycles at 0.05 A g^{-1}. Cyclic voltammetry (CV) measurements were performed using a VSP-3e Biologic potentiostat/galvanostat within the same voltage window as GC, at a constant scan rate of 0.1 mV s^{-1}. Electrochemical impedance spectroscopy (EIS) was conducted using a Biologic BCS-805, within a frequency range of 10 kHz to 20 mHz, applying a potential amplitude of 10 mV. EIS measurements were conducted intermittently during GC at different cycle numbers.

The surface morphology of the pristine C45/binder electrodes was analysed using FESEM with an Auriga dual-beam FIB-SEM workstation (Zeiss).

3. Results and discussion

3.1. CNCs synthesis and characterization

The three typologies of nanocrystals under investigation were prepared from Avicel PH101. Fig. 1 schematically represents the preparation of the three CNCs typologies from the cellulose source. S-CNCs were prepared by H_2SO_4 hydrolysis. This approach utilizes H_2SO_4 64 % in water at moderate temperatures (i.e., 45 °C) and typically produces the desired nanostructured materials in low yield (15 % for the reaction batch used in this work) [29,38]. Neutral cellulose nanocrystals, instead, can be produced either by HCl hydrolysis (giving N—CNC) [27], or mechano-enzymatic hydrolysis (obtaining eN—CNC) [29]. HCl hydrolysis requires higher temperature (i.e., 105 °C) and 6 h of reaction time. Depending on the batch, also this method can give unsatisfactory results in terms of reaction yield (21 % for the batch used in this work). Conversely, the mechano-enzymatic hydrolysis represents an interesting approach for the preparation of cellulose nanostructures, since it avoids the use of concentrated mineral acids and disposal of toxic or corrosive waste as in the previous two cases, and leads a higher yield (76 %) and more reproducible results. In this case, the endoglucanase from *Aspergillus niger* is used to catalyze the hydrolysis reaction in a phosphate buffer at pH 5.0 as dispersing medium. To favor enzyme access to cellulose fibers, a mild mechanic pretreatment is applied to Avicel before the hydrolysis reaction, using a horizontal ball mill equipped with stainless steel jars. Table 1 summarizes the reaction yields for the three nanocrystal types along with their calculated E-factors, defined as the ratio of the total mass of waste generated to the mass of the isolated pure product. The E-factor is a key metric for evaluating the environmental impact and sustainability of chemical processes: lower values indicate more efficient and environmentally friendly methods. Comparison of the calculated E-factors highlights a marked difference among the three CNC preparation routes. The mechanical-enzymatic pathway for eN—CNC exhibits an exceptionally low E-factor (0.7), far below those of acid-based methods (14.9 for hydrochloric acid and 36.4 for sulfuric acid). This outcome underscores the superior efficiency of the enzymatic approach, which operates under mild conditions, avoids concentrated mineral acids, and minimizes waste generation during both reaction and purification stages.

Nanocrystals were characterized by elemental analyses, ATR-FTIR, FESEM-EDS, and XRD. Table 1 collects the elemental analysis results of the three samples, in which the carbon content is in line with the expected value. Indeed, the lower carbon percentage found in each sample with respect to the theoretical cellulose value (44.45 %) is due to the crystallized water content naturally present in CNCs. As expected, the sulfur content in S-CNC is higher than in neutral CNCs. We calculated a substitution degree with sulfate groups in S-CNC equal to ~0.03, according to a previously described procedure [39]. The enzymatic CNCs, instead, present 0.25 % of nitrogen, due to the presence of traces of enzyme in the purified material (on average ~2.5 % of total weight of eN—CNC, based on average aminoacid molecular weight). Additional confirmation of nanocrystal purity is provided by SEM-EDS analyses (**Tables S1-S3**), which clearly show that the enzymatic nanocrystals possess a clean elemental profile, with no detectable residual phosphorus from the hydrolysis reaction.

ATR-FTIR spectra of the three compounds are reported in Fig. 2. No significant difference could be noticed between the samples. In all cases, the characteristic cellulose peaks are evident, such as the O—H stretching at 3325 cm^{-1} and the C—OH one at 1025 cm^{-1}. Furthermore, a weak signal of the deformation mode of anomeric CH is evident at 896 cm^{-1}. The signal of the bending mode of crystallized water in each sample falls at 1646 cm^{-1}. No evident signal of protein residue presence in eN—CNC could be detected by this spectroscopic technique.

Crystallinity indexes of cellulose nanocrystals are included in Table 1. The XRD pattern of the three samples are reported in Fig. 3. The distinctive peaks of the diffractogram corresponding to cellulose I, the crystalline allomorph of cellulose found in plants, were identified in each sample. Diffraction patterns are plotted against an absolute axis on momentum transfer Q. Crystallinities were calculated from XRD pattern by the Segal method, considering the ratio $CrI = (I_{200} - I_{am})/I_{200}$, where I_{200} represents the maximum intensity of the peak with Miller's indexes 200 (centered at 1.6Q in our spectra, and corresponding to 22.6° in the 2θ axis when $CuK_{\alpha 1}$ radiation is used), while the intensity of the amorphous peak is found at 1.3Q for cellulose I. The higher crystallinity found for S-CNC (i.e., 80.0 %) reflects the efficiency of H_2SO_4 in digesting amorphous cellulose regions. However, the other two samples have very close crystallinity values and reveal the feasibility of using neutral cellulose nanocrystals in several applications, especially considering the high yield obtained in the case of mechano-enzymatic hydrolysis.

Fig. 4 collects the FESEM images of nanocrystals deposited from 1 mg L^{-1} suspensions in DMSO. In all cases, the morphology of the materials is in line with the expected dimension of cellulose nanocrystals (approximately 100 nm long). It is evident the aggregation behaviour of the three typologies of nanocrystals, tending in all cases to form aggregates interacting by their long side, with neutral CNCs (both acid and enzymatic) forming nanocrystal clusters rather than thin films, as in the case of S-CNC.

3.2. Binders electrochemical stability

In order to evaluate the electrochemical stability of the synthesized binders, CVs were carried out in the potential range of 0.01–3 V vs K^+/K. The voltammograms corresponding to cycles 1 to 5 of the CNCs binder electrodes are shown in Fig. 5. For the sake of comparison, the same protocol was adopted for a T-cell a with bare aluminum electrode. As observed, all CNCs-based binders exhibited remarkable stability within

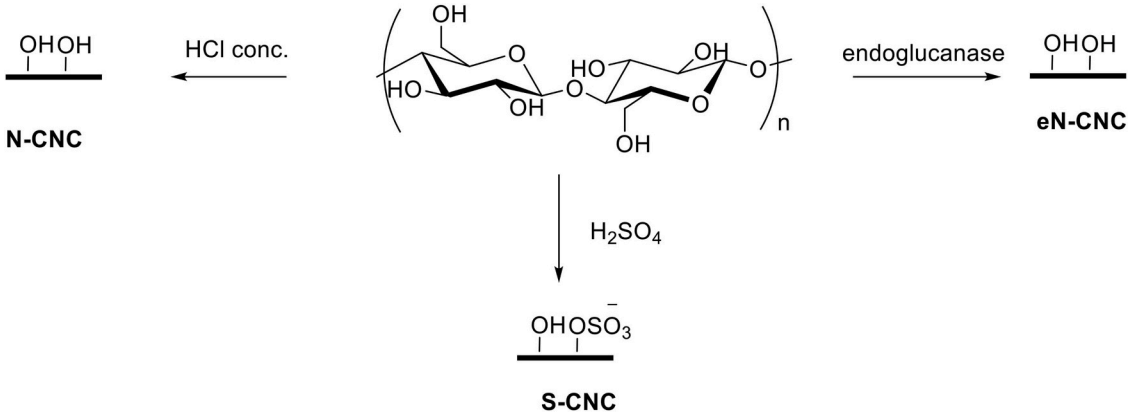


Fig. 1. Synthesis of cellulose nanocrystals from Avicel by different hydrolytic approaches.

Table 1
Reaction yield, E-factor, elemental analyses, and crystallinity indexes of the three CNCs samples. [(a)] Determination of oxygen weight percentage was done by difference.

	Yield	E-factor	Elemental analysis (% w/w)					Crystallinity index
			C	H	N	S	O[(a)]	
N-CNC	21 %	14.9	40.81	6.12	0	0.02	53.05	76.3 %
eN—CNC	76 %	0.7	41.03	6.13	0.25	0.04	52.55	76.9 %
S-CNC	15 %	36.4	40.11	6.55	0	0.6	52.74	80.0 %

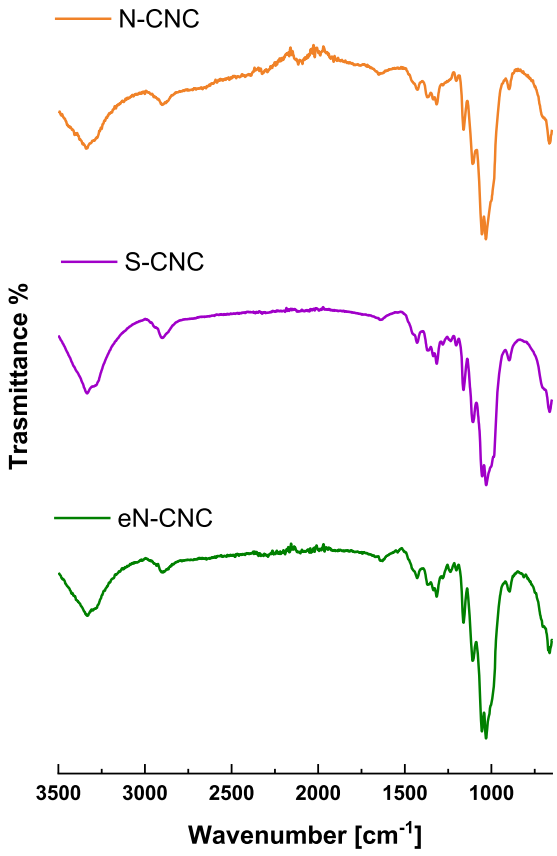


Fig. 2. ATR-FTIR spectra of neutral cellulose nanocrystals obtained by acid and enzymatic hydrolysis, respectively, in orange and green lines, and sulfated cellulose nanocrystals in violet line.

the working potential window. The CV curves of the CNCs binders are very similar to each other, with no significant redox processes detected after the first cycle. During this cycle, a reduction peak is centered at around 0.65 V, which is associated with the formation of the solid electrolyte interphase (SEI) layer products [37]. Indeed, this peak is also present in the voltammogram of the bare Al electrode (Fig. 5**d**), indicating that it is not related to any irreversible reactions of the binders rather than of liquid electrolyte. After the first cycle, the CV curves stabilize and nearly overlap in subsequent cycles, indicating the stability of the synthesized binders. The current was normalized to the combined mass of the binder and aluminum to allow comparison among the different cells. As it can be seen, intensity in all voltammograms remained very low and nearly identical across the four cells. This satisfactorily confirms that the binders are not electrochemically active within the explored potential window. Furthermore, it indicates that they do not catalyze electrolyte decomposition or contribute to side reactions, as long as they are not in contact with the carbon black. A more detailed evaluation of their behavior in composite carbon electrodes will be discussed in the following sections.

3.3. Electrochemical evaluation and morphological characterization of C45/binder electrodes

To study the electrochemical performance of the synthesized CNCs as binders within a realistic electrode formulation, C45 was selected as the active carbon material due to its proven performance as both an active material and conductive additive in LIBs and KIBs [37,40]. Moreover, previous studies have shown the compatibility of this carbon material with cellulose-derived binders [37,41]. **Figure S1** displays photographs of the coatings obtained with each CNC binder. These images demonstrate the high adhesion of the slurries to the current collectors, as evidenced by the sharp edges of the electrode discs, which remain intact after cutting with no significant material detachment.

Fig. 6**a** and **Figure S2a** show the results of the GC characterization. As it can be observed, all the materials exhibited excellent cycling stability and specific capacities consistent with values reported in literature for similar systems [42]. Although the four electrodes delivered comparable capacities during the first 20 cycles, clear differences emerged afterwards: the C45/CNCs electrodes outperformed the C45/CMC electrode, with C45/eN—CNC achieving the highest capacity overall. Remarkably, it should be noted that the commercial C45/CMC electrode exhibited a slight fluctuation in specific capacity values between cycles 20 and 45, while the C45/CNC electrodes showed remarkable stability and capacity retention beyond the initial cycles. The Coulombic efficiencies (CE) of the four C45/binder electrodes were evaluated and shown in **Figure S2b**. While the initial CE for all electrodes is notably low (approximately 40 %), values rise sharply to ~90 % after only one cycle. Efficiencies continue to improve, exceeding 98 % after 10 cycles and stabilizing near 99 % by the 20th cycle.

Fig. 6**b** shows the bar graph of the specific discharge capacity fading of each cycle with respect to the previous one, for the first five cycles. The largest irreversible capacity fading took place between the first and the second cycle, and this can be attributed to the formation of the SEI layer [43]. However, as shown in the figure, the capacity fading rapidly decreased over the subsequent cycles, resulting in only a minor loss between 1 % and 3 % at the 5th cycle. The electrode with the highest capacity fading (and therefore the lowest reversibility) is C45/CMC. In contrast, the C45/CNC electrodes demonstrated improved reversibility, with C45/eN—CNC showing the lowest capacity decay from the third cycle on. This trend is further confirmed by the data presented in **Figure S2c**, which shows capacity retentions at the 100th cycle with respect to the capacity at the 5th cycle. The C45/CMC electrode exhibited the lowest capacity retention (81 %), followed by C45/N—CNC and C45/S-CNC (both with 93 %), while C45/eN—CNC achieved the highest retention of 97 %. These results can be attributed to differences in surface chemistry and functional groups between CNCs and CMC. Neutral CNC produced by enzymatic hydrolysis (eN—CNC) presents a cleaner surface and with minimal surface charges, free from sulfate or other ionic functional groups that could negatively affect electrochemical stability. This neutral and aggregated surface minimizes side reactions with the electrolyte and potassium ions, which would otherwise catalyze electrolyte decomposition and degrade the

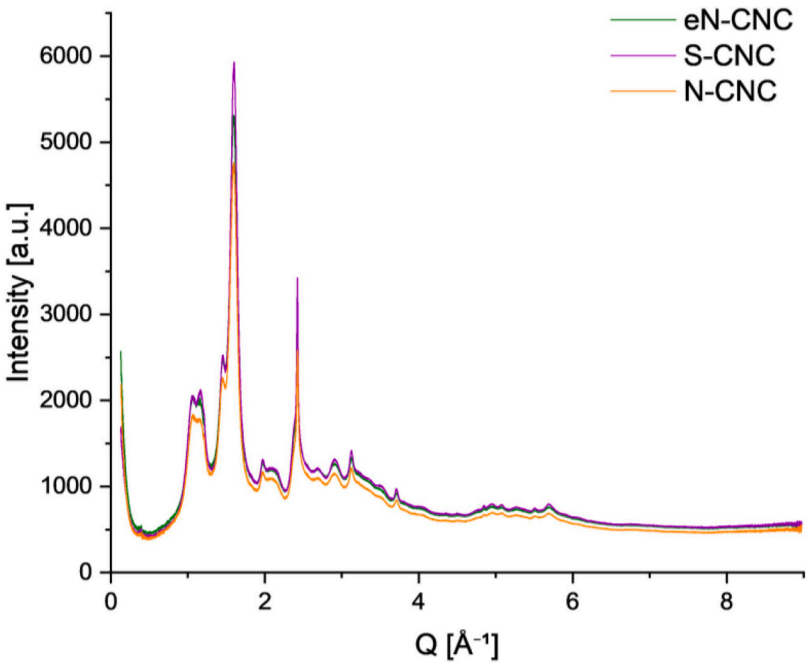


Fig. 3. Diffractograms of N—CNC, eN—CNC, and S-CNC.

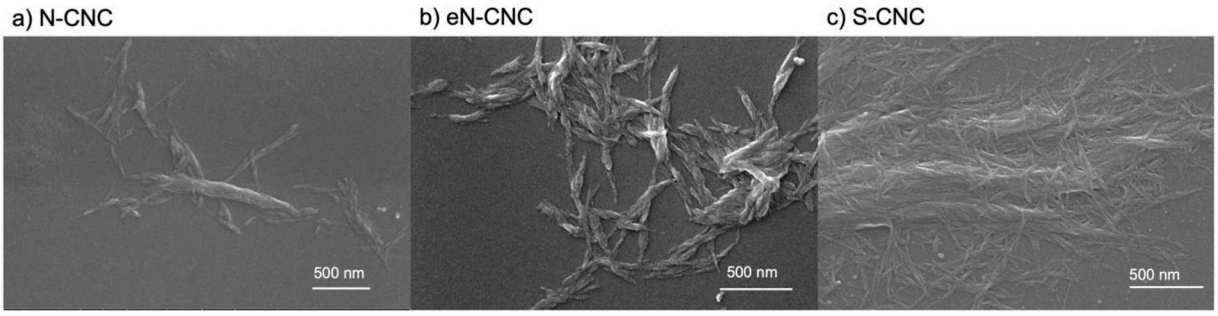


Fig. 4. FESEM micrographs of: a) N—CNC; b) eN—CNC; c) S-CNC, acquired on samples deposited on glass from 1 mg L^{-1} DMSO suspensions.

electrode/electrolyte interface. By limiting these undesired interactions, as done for CNCs, stable cycling behavior and reduced capacity fading are more easily achieved.

The voltage profiles of the C45/binder electrodes during GC are presented in Fig. 7. Excluding the first cycle, all profiles exhibited a similar shape characteristic of pseudocapacitive charge storage, marked by the absence of well-defined plateaus [44]. These pseudocapacitive materials store charge through Faradaic processes that predominantly occur at the surface of the electrode rather than within the bulk [44]. This behavior has been previously reported for carbon anodes using C45 as active material, indicating that the use of CNCs-based binders does not alter the intrinsic charge storage mechanism [37]. It should also be noticed that, from the second cycle onward, the voltage profiles of all electrodes nearly overlap, indicating excellent cycling stability and minimal occurrence of irreversible reactions.

When comparing the first and second cycles of each electrode, significant differences were observed in both profile shape and specific capacity, mainly attributed to the formation of the SEI layer during the initial cycle [43]. Notably, in the first cycle, the C45/CNCs electrodes displayed a voltage plateau at around 0.65 V, that was absent in the C45/CMC cell, suggesting distinct SEI layer formation mechanisms depending on the binder employed. This is consistent with previous studies showing that binder selection can influence the starting potential of electrolyte reduction and the composition of the resulting SEI layer [45].

Additionally, it can be observed that the C45/CMC electrode exhibited the highest initial specific discharge capacity (i.e., 468 mAh g^{-1}), while the C45/CNCs electrodes showed lower capacities ranging from approximately 250 to 300 mAh g^{-1}. However, despite its high initial capacity, the C45/CMC electrode underwent a sharp capacity drop in the second cycle (as shown in Fig. 6**b**), indicating that much of the first cycle capacity was associated with irreversible processes. In contrast, the C45/CNC electrodes displayed more moderate initial capacities, followed by improved reversibility and stable cycling behavior. This kind of achievement is crucial for the development of future potassium-ion full cells, where the potassium ions amount is not practically unlimited as in the half-cells with potassium metal as anode (used in this work); it will be of vital importance not to waste so many potassium ions in side and decomposition reactions ascribed to the SEI layer formation.

Fig. 8 shows the cyclic voltammograms from the 1st to the 5th cycle for the four different C45/binder electrodes. In the case of the C45/CNCs cells, all the three electrodes exhibited very similar electrochemical behavior. During the first reduction scan, a pronounced peak appeared at approximately 0.65 V, which correlates with the electrolyte decomposition detected by the plateau in the galvanostatic profiles of Fig. 7 and the CV peaks shown in Fig. 5. This peak has been widely reported for carbon electrodes with both cellulose- and PVDF-based binders and is

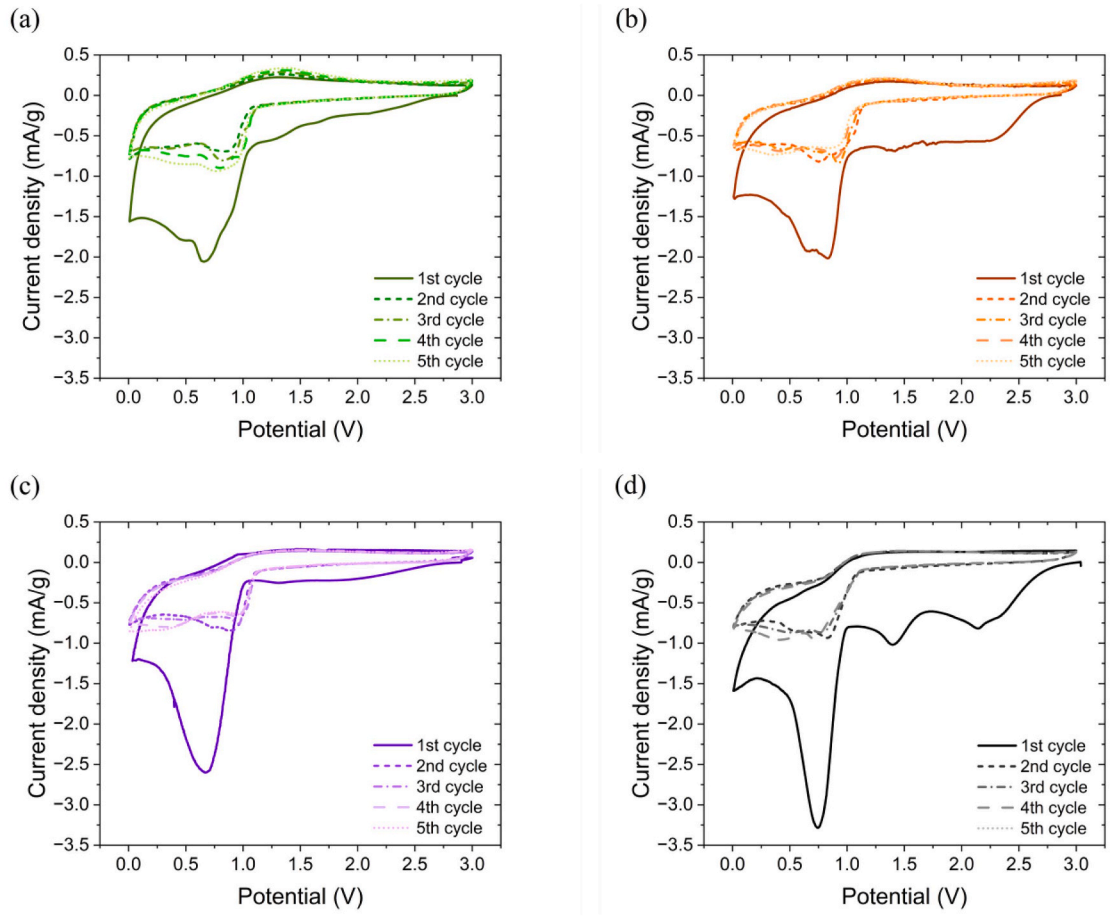


Fig. 5. CV at 0.1 mV s^{-1} of binder electrodes: (a) eN—CNC, (b) N—CNC, (c) S-CNC; (d) bare aluminum. The current is normalized to the total mass of the binder and the aluminum current collector to allow comparison among the different cells.

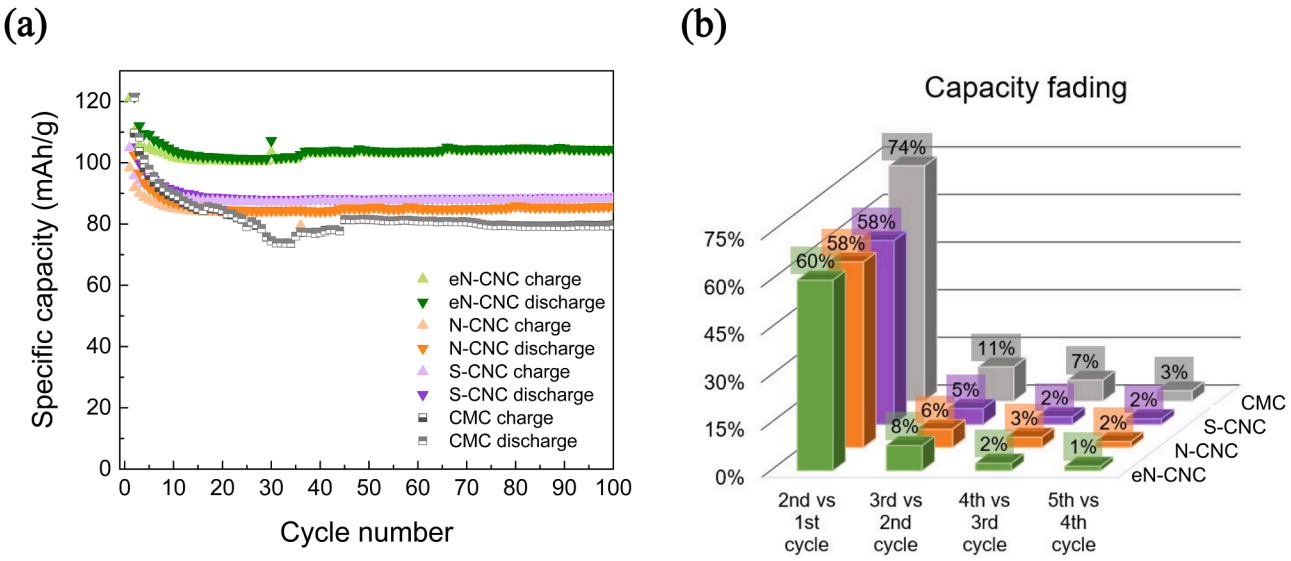


Fig. 6. (a) Galvanostatic cycling performance at 0.05 A g^{-1} of half-cells assembled with the four different C45/binder electrodes (excluding the first cycle). (b) Bar graph of specific discharge capacity fading over different cycle numbers for the four different C45/binder electrodes.

typically associated with the SEI layer formation [46,47]. In contrast, the C45/CMC cell also exhibited a signal in this region, although less sharply defined, which is consistent with previous reports [37,47]. All cells also displayed a large irreversible slope in the low potential region (0.3–0.01 V) during the first reduction scan, attributed to three storage mechanisms: K^+ intercalation into the carbon matrix, ion adsorption on the surface, and pore filling [48–50]. The corresponding first oxidation branch presented a peak located at around 0.5 V, which can be related to the K-ion deintercalation process.

From the second cycle onward, all the CV curves exhibited a highly

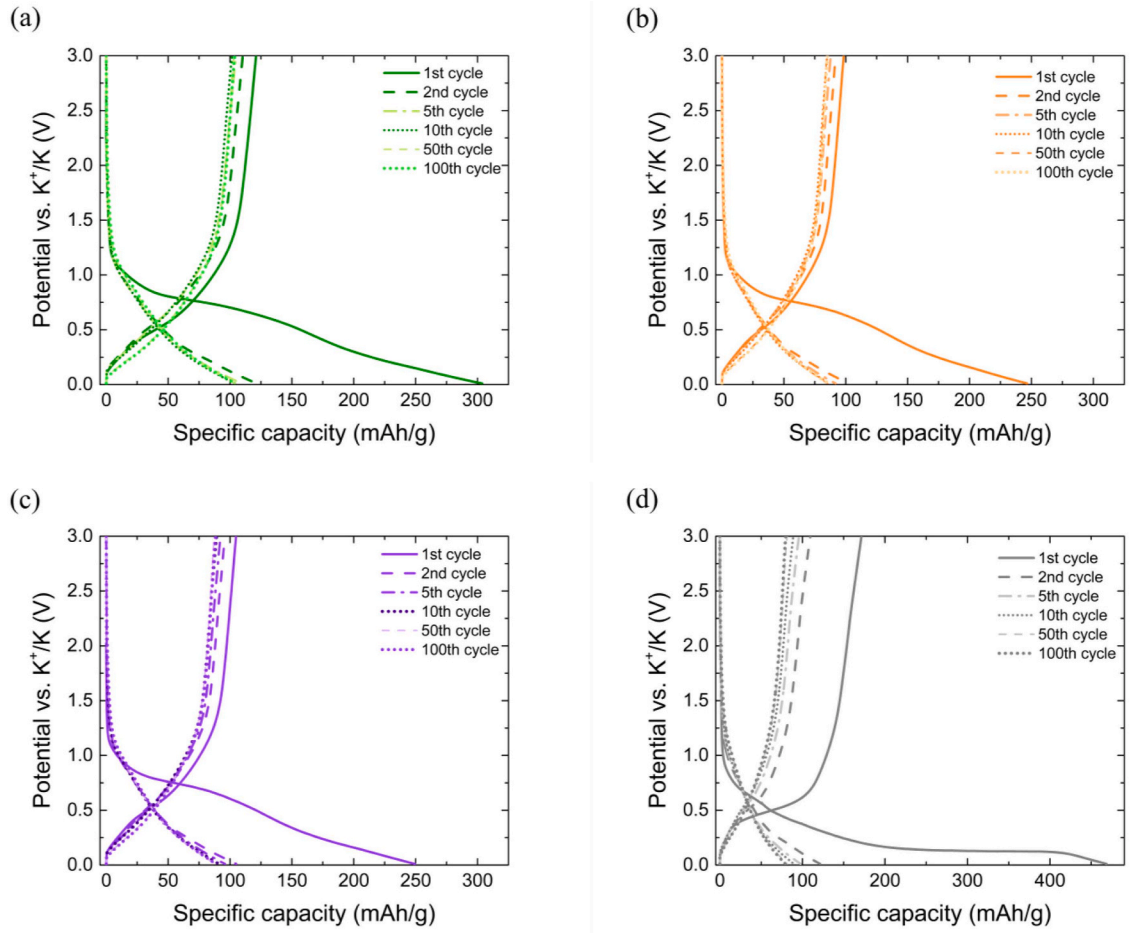


Fig. 7. Galvanostatic charge and discharge profiles at different cycle numbers (at 0.05 A g^{-1}) for (a) C45/eN—CNC, (b) C45/N—CNC, (c) C45/S-CNC, and (d) C45/CMC.

reproducible behavior, almost overlapping among them. The reduction branches presented two broad peaks. The first one, between 1.3 and 0.5 V, corresponds to the surface-driven redox reactions. The second one, located between 0.5 and 0.01 V, reflects bulk diffusion and insertion of potassium ions into the carbon matrix.

Moving on to the oxidation branch, it can be observed that the four C45/binder electrodes exhibited a broad low-potential peak at approximately 0.25 V, which intensifies from the second cycle onward, and a second peak centered at ~0.6 V. This dual-peak behavior has been previously reported for C45/CMC electrodes and was attributed to a two-step depotassiation process, involving both bulk ion deintercalation and surface ion release [37].

Figure S3 compares the second CV cycle of each C45/CNC electrode with the same cycle number of each corresponding binder electrode. As shown, the contribution of the binders to the overall current is negligible, confirming that the electrochemical response in the C45/CNC electrodes mainly corresponds to the active carbon material.

EIS measurements were carried out on the C45/binder electrodes during galvanostatic cycling at 0.05 A g^{-1}. Fig. 9 shows a comparison of the EIS spectra of the electrodes in three representative states: pristine (a), after one cycle (b), and 100 cycles (c). Each Nyquist plot features a depressed semicircle in the high-to-mid frequency region, attributed to the charge transfer resistance (R_{ct}) and the surface film impedance, followed by a sloped line at low frequencies associated with potassium iojns diffusion. The semicircle diameter serves as a measure of R_{ct} at the electrode/electrolyte interface. As it can be seen, a remarkable decrease in R_{ct} was observed after cycling, indicating an improvement in charge transfer kinetics likely due to the formation of a stable and more conductive SEI layer. This trend has previously been reported for carbon anodes in KIBs using KFSI as electrolyte salt [51]. It should be noted that, in all cases, the C45/CNC electrodes exhibited lower R_{ct} values compared to C45/CMC, suggesting that CNC-based binders promoted more efficient charge transfer. This behavior indicates that the binders produced from neutral cellulose nanocrystals provide a highly effective physical network that binds carbon particles tightly, enhancing the electrical conductivity while maintaining strong adhesion to the current collector. The capacity of nanocelluloses to effectively interact with carbon particles, disrupting their aggregates, has been already reported in the literature [52,53].

Figure S4 expands this analysis by showing Nyquist plots at additional cycling stages. The data reveal that the most pronounced decrease in R_{ct} occured between the pristine state and the first cycle, with only minor changes thereafter. Additionally, the general shape of the impedance spectra does not significantly change after the first cycle, suggesting a stable SEI layer formation and unchanged charge-storage kinetics over extended cycling. As it can be observed, the depressed semicircle in the pristine electrodes is followed by a nearly vertical line in the low-frequency region. This behavior is typical of fresh electrodes and it is associated with a double-layer capacitance where ions adsorb at the surface without significant intercalation into the bulk [53–55]. Upon cycling, this profile transitions into a semicircle followed by a line with a slope of approximately 45°, indicative of diffusion-limited processes. This evolution further confirms the formation of a stable SEI layer and the progressive intercalation of K^+ into the carbon matrix, which alters the shape of the impedance response.

The composition of the electrode binder can significantly influence

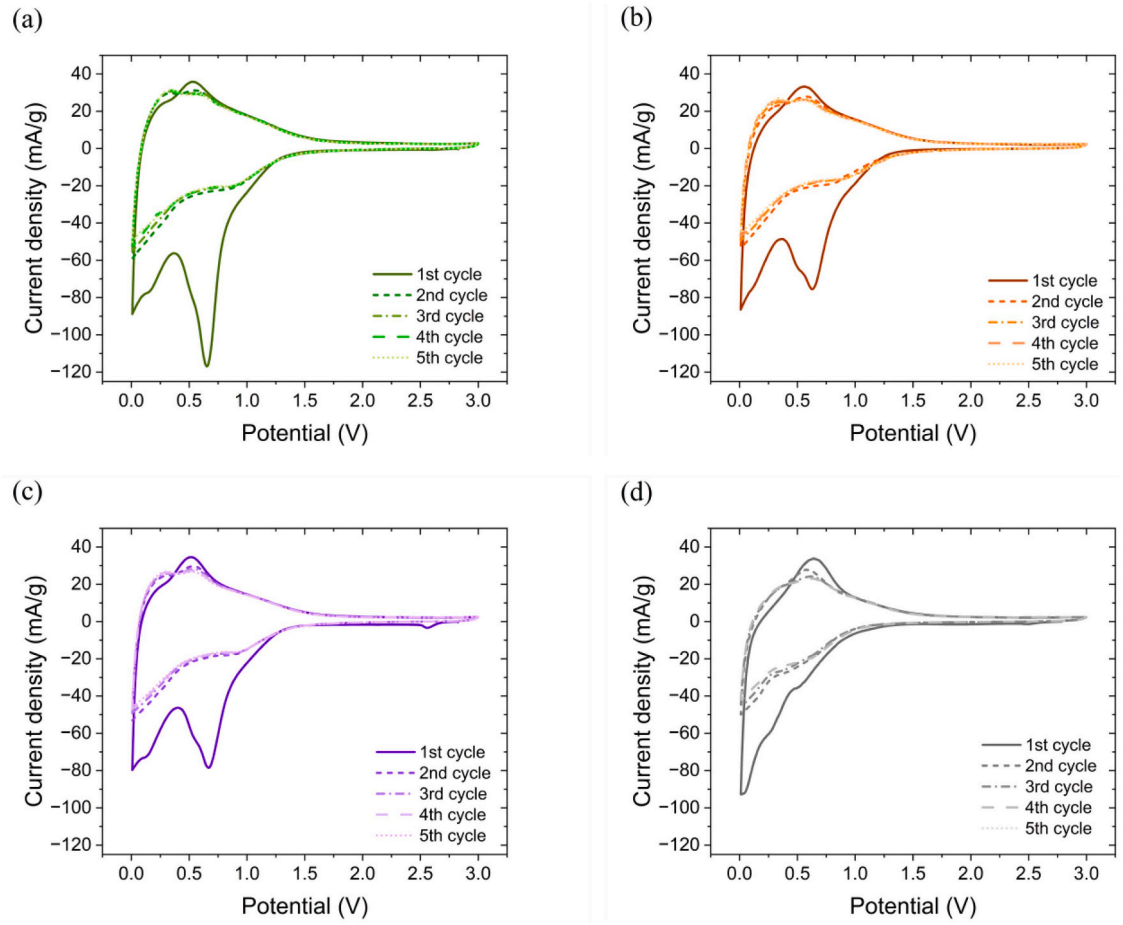


Fig. 8. CV voltammograms at 0.1 mV s^{-1} of the C45/binder electrodes: (a) C45/eN—CNC, (b) C45/N—CNC, (c) C45/S-CNC, and (d) C45/CMC. The current is normalized to the mass of the active material (C45).

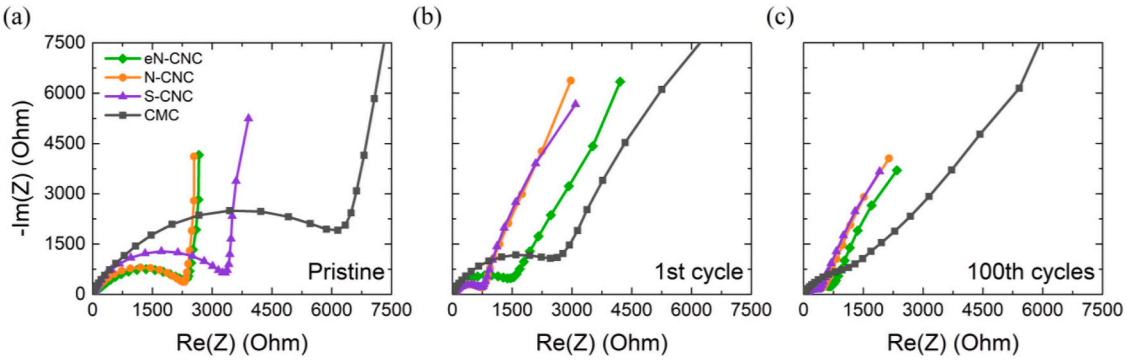


Fig. 9. Nyquist plots obtained with the EIS measurements for the four C45/binder electrodes after different galvanostatic cycling at 0.05 A g^{-1}: (a) pristine electrodes, (b) after the first cycle, and (c) after 100 cycles.

reaction kinetics, leading to different electrochemical responses [45]. To evaluate this effect, the rate capability of the C45/CNC electrodes was measured, and the results are presented in **Figure S5**. As shown, all electrodes exhibited similar capacity retention across the tested C-rates. It should be noted that, when the current density returned to the lowest value after high-rate cycling, the capacity was fully recovered. This demonstrated the excellent reversibility of the C45/CNC electrodes and underscored the ability of CNCs binders to withstand high currents without mechanical degradation. Notably, C45/eN-CNC consistently delivered the highest specific capacity at each current density.

In order to better understand the differences among the electrochemical responses of the C45/CNCs electrodes, morphological characterizations of the pristine electrodes were carried out and the results are shown in Fig. 10. At low magnification (Fig. 10**a–c**), it can be observed that all the electrodes present a fairly homogenous surface with well-distributed active carbon particles and without perceptible agglomerations. However, the C45/N-CNC (Fig. 10**b**) and especially the C45/S-CNC (Fig. 10**c**) electrodes display visible surface cracks, whereas the C45/eN-CNC electrode remains crack-free and appears notably smoother. Looking at the higher magnification micrographs (Fig. 10**d–f**), residual CNCs particles are evident on all electrodes, but those on the C45/S-CNC sample are noticeably larger. Such

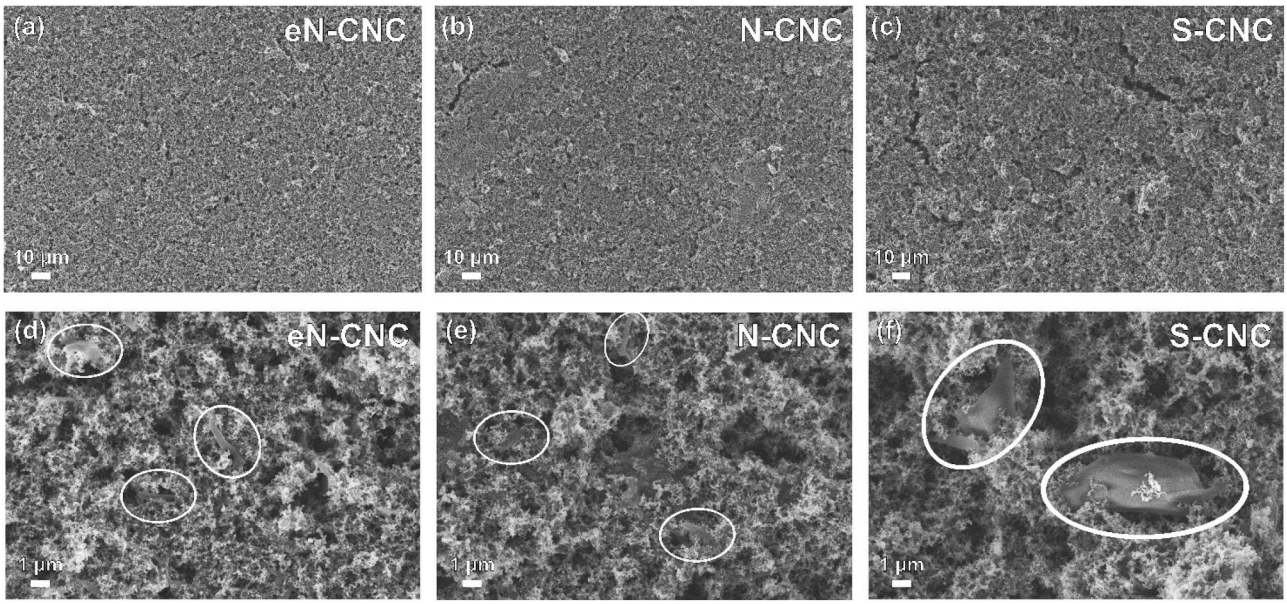


Fig. 10. FESEM images at two magnification levels of C45/CNCs electrodes: (a) and (d) C45/eN—CNC, (b) and (e) C45/N—CNC, and (c) and (f) C45/S-CNC.

morphological differences likely contribute to the observed variation in the electrochemical performance.

The surface chemistry of the binders could explain these differences among the electrodes morphology. On one hand, the negatively charged sulfate groups on S-CNC may induce electrostatic repulsion with the carbon surface, leading to weaker binder–carbon interaction and facilitating crack formation. On the other hand, neutral CNCs exhibit a homogeneous charge distribution, yielding a more stable surface.

4. Conclusions

In this study, we have synthesized and characterized three types of CNCs produced via different hydrolysis methods. The mechano-enzymatic approach has revealed the highest reaction yield, the lowest E-factor, and the formation of CNCs with good purity and crystallinity properties. The high yield makes the mechano-enzymatic approach very competitive with respect to the benchmark preparation methods based on the use of inorganic acids (sulfuric or hydrochloric acids). Furthermore, we have synthesized both nanocrystals characterized by surface sulfation (S-CNC) and nanocrystals composed of pure cellulose (N—CNC and eN—CNC), and demonstrated that the synthesized CNCs serve as effective, sustainable binder materials for carbon anodes in KIBs. CV on bare binder electrodes confirmed that all three CNCs samples exhibited excellent electrochemical stability within the 0.01–3 V region vs. K^+/K, with negligible redox activity beyond the initial SEI layer formation. The electrochemical characterizations carried out on CNCs-based carbon electrodes prepared with Super C45 activa material evidenced that the C45/CNC electrodes outperformed those prepared using the commercially available CMC binder.

Among the explored CNCs variants, C45/eN-CNC electrodes stood out by delivering the highest specific capacities, best capacity retention (97 % after 100 cycles), and the most homogeneous electrode surface. This superior performance is attributed to its neutral surface chemistry, which minimizes undesired side reactions and enables the formation of a stable SEI layer. N-CNC and S-CNC also outperformed CMC in terms of cyclability and impedance, though S-CNC ionic surface groups led to slight mechanical irregularities. Overall, our findings underscore the promise of CNCs (particularly the enzymatically produced one, neutral nanocrystals) as green, cost-effective alternatives to both PVDF and conventional cellulose derivatives for KIB electrodes.

CRediT authorship contribution statement

Sofia Raviolo: Writing – original draft, Methodology, Investigation, Formal analysis, Data curation, Conceptualization. **Rosarita D'Orsi:** Writing – original draft, Methodology, Investigation, Formal analysis, Data curation, Conceptualization. **Sabrina Trano:** Writing – review & editing, Supervision, Resources, Project administration. **Laura Spagnuolo:** Writing – review & editing, Validation, Investigation. **Matteo Cei:** Writing – review & editing, Validation, Investigation, Data curation. **Alessandra Operamolla:** Writing – review & editing, Supervision, Resources, Project administration, Funding acquisition, Conceptualization. **Federico Bella:** Writing – review & editing, Visualization, Supervision, Resources, Project administration, Funding acquisition.

Declaration of competing interest

The authors declare that they have no known competing financial interests or personal relationships that could have appeared to influence the work reported in this paper.

Acknowledgments

This study was carried out within the GREEN2MOVE project [FISA-2022–00983] funded by Ministero dell'Università e della Ricerca (Bando FISA 2022). R.D. and A.O. acknowledge the University of Pisa for the funding “BIHO 2022 – Bando Incentivi di AteneoHorizon e Oltre” (Prot. n. 0048740/2022). L.S. acknowledges Ministero dell'Università e della Ricerca for the project PON 2014–2020 (D.M. 1061/2021, CUP I59 J21017690008) entitled “Conversion of lignocellulosic biomass into cellulose fibers, lignin, and active biomolecules for the preparation of smart and sustainable coating for textiles of natural origin and similar flexible substrates”. The authors thank CISUP (Center for Instrument Sharing of the University of Pisa) for the access to the FESEM facility. AO acknowledges the ESRF for provision of synchrotron radiation facilities and Momentum Transfer for facilitating the measurements. Jakub Drnec is thanked for assistance and support in using beamline ID31. The measurement setup was developed with funding from the European Union’s Horizon 2020 research and innovation program under the STREAMLINE project (grant agreement ID 870313). Measurements performed as part of the MatScatNet project were supported by OSCARS through the European Commission Horizon Europe Research and

Innovation programme under grant agreement no 101129751.

Supplementary materials

Supplementary material associated with this article can be found, in the online version, at doi:10.1016/j.apmt.2026.103155.

Data availability

Data will be made available on request.

References

[1] X.-Q. Zhang, C.-Z. Zhao, J.-Q. Huang, Q. Zhang, Recent advances in energy chemical engineering of next-generation lithium batteries, Engineering 4 (2018) 831–847, https://doi.org/10.1016/j.eng.2018.10.008.

[2] A. Benigno, S. Raviolo, S. Trano, S. Domenici, M. Castellino, C. Francia, D. Gaspar, L. Pereira, F. Bella, From biomass to battery: lignin-derived carbons achieving unprecedented high capacity retention in potassium batteries, Chem. Eng. J. 528 (2026) 172142, https://doi.org/10.1016/j.cej.2025.172142.

[3] A. Sattar, N. Shahzad, M.A. Tariq, T. Yousaf, S. García-Ballesteros, M.I. Shahzad, R. Liaquat, M. Ali, F. Bella, Role of bifunctional additives towards highly efficient and stable tin perovskite solar cells, Mater. Today Energy 53 (2025) 101986, https://doi.org/10.1016/j.mtener.2025.101986.

[4] M. Murugavel, A.K. Lakshmi, N. Angulakshmi, S. García-Ballesteros, F. Bella, A. M. Stephan, Viologen as an electrolyte additive for extreme fast charging of lithium-ion batteries, Battery Energy 4 (2025) e20240039, https://doi.org/10.1002/bte2.20240039.

[5] B. Bertoncini, A. Taddeucci, S. Trano, S. Raviolo, I. Valdrighi, F.M. Vivaldi, V. Mattoli, F. Bella, M. Carlotti, A multipotent precursor approach for the preparation of high-molecular weight conjugated polymers with redox active units, Small Methods 9 (2025) 2500488, https://doi.org/10.1002/smtd.202500488.

[6] N. Pirrone, S. García-Ballesteros, J. Amici, M. Castellino, S. Hernández, F. Bella, Chemometrics-boosted protocols for effortless evaluation of factors affecting the electrochemical nitrate reduction to ammonia, J. Energy Chem. 107 (2025) 599–611, https://doi.org/10.1016/j.jechem.2025.03.072.

[7] L.A. Kumar, M. Murugavel, S. Alwarappan, F. Bella, A.M. Stephan, Fast charging of lithium-ion batteries by the effective formulation of nonaqueous liquid electrolytes, J. Phys. Chem. C 129 (2025) 9980–9991, https://doi.org/10.1021/acs.jpcc.5c00374.

[8] S. Domenici, R. Speranza, F. Bella, A. Lamberti, T. Gatti, A sustainable hydrogel-based dye-sensitized solar cell coupled to an integrated supercapacitor for direct indoor light-energy storage, Solar RRL 9 (2025) 2400838, https://doi.org/10.1002/solr.202400838.

[9] G. Pascuzzi, S. Trano, C. Francia, S. Turri, F. Bella, G. Griffini, Elucidating the interplay between structure and electrochemical behavior in lignin-based polymer electrolytes for potassium batteries, Battery Energy 4 (2025) e70002, https://doi.org/10.1002/bte2.70002.

[10] A. Mangini, A. Garbujo, P. Biasi, V. Testa, M.C. Bruzzoniti, L. Rivoira, S. Garcia-Ballesteros, F. Bella, Debunking pitfalls of Li–N_2 cells for ammonia electroproduction: is this setup affordable to prove nitro-fixation before lithium plating? ACS Electrochem. 1 (2025) 2866–2877, https://doi.org/10.1021/acselectrochem.5c00402.

[11] P. Prete, S. Trano, P. Zaccagnini, L. Fagiolari, J. Amici, A. Lamberti, A. Proto, F. Bella, R. Cucciniello, Glycerol carbonate and solketal carbonate as circular economy bricks for supercapacitors and potassium batteries, ChemSusChem 17 (2024) e202401636, https://doi.org/10.1002/cssc.202401636.

[12] K. Kubota, M. Dahbi, T. Hosaka, S. Kumakura, S. Komaba, Towards K-ion and Na-ion batteries as 'beyond Li-ion, Chem. Rec. 18 (2018) 459–479, https://doi.org/10.1002/tcr.201700057.

[13] R. Rajagopalan, Y. Tang, X. Ji, C. Jia, H. Wang, Advancements and challenges in potassium ion batteries: a comprehensive review, Adv. Funct. Mater. 30 (2020) 1909486, https://doi.org/10.1002/adfm.201909486.

[14] S. Komaba, T. Hasegawa, M. Dahbi, K. Kubota, Potassium intercalation into graphite to realize high-voltage/high-power potassium-ion batteries and potassium-ion capacitors, Electrochem. Commun. 60 (2025) 172–175, https://doi.org/10.1016/j.elecom.2015.09.002.

[15] Y. Matsuda, H. Nakashima, M. Morita, Y. Takasu, Behavior of some ions in mixed organic electrolytes of high energy density batteries, J. Electrochem. Soc. 128 (1981) 2552–2556, https://doi.org/10.1149/1.2127289.

[16] M. Okoshi, Y. Yamada, S. Komaba, A. Yamada, H. Nakai, Theoretical analysis of interactions between potassium ions and organic electrolyte solvents: a comparison with lithium, sodium, and magnesium ions, J. Electrochem. Soc. 164 (2017) A54–A60, https://doi.org/10.1149/2.0211702jes.

[17] J. Zhao, X. Zou, Y. Zhu, Y. Xu, C. Wang, Electrochemical intercalation of potassium into graphite, Adv. Funct. Mater. 26 (2016) 8103–8110, https://doi.org/10.1002/adfm.201602248.

[18] X. Wu, Z. Xing, Y. Hu, Y. Zhang, Y. Sun, Z. Ju, J. Liu, Q. Zhuang, Effects of functional binders on electrochemical performance of graphite anode in potassium-ion batteries, Ionics (Kiel) 25 (2019) 2563–2574, https://doi.org/10.1007/s11581-018-2763-4.

[19] J. Wu, Q. Zhang, S. Liu, J. Long, Z. Wu, W. Zhang, W.K. Pang, V. Sencadas, R. Song, W. Song, J. Mao, Z. Guo, Synergy of binders and electrolytes in enabling microsized alloy anodes for high performance potassium-ion batteries, Nano Energy 77 (2020) 105118, https://doi.org/10.1016/j.nanoen.2020.105118.

[20] Y. Ma, J. Ma, G. Cui, Small things make big deal: powerful binders of lithium batteries and post-lithium batteries, Energy Storage Mater 20 (2019) 146–175, https://doi.org/10.1016/j.ensm.2018.11.013.

[21] S. Sudhakaran, T.K. Bijoy, A comprehensive review of current and emerging binder technologies for energy storage applications, ACS Appl. Energy Mater. 6 (2023) 11773–11794, https://doi.org/10.1021/acsaem.3c02218.

[22] C. Wang, L. Su, N. Wang, D. Lv, D. Wang, J. Yang, Y. Qian, Unravelling binder chemistry in sodium/potassium ion batteries for superior electrochemical performances, J. Mater. Chem. A 10 (2022) 4060–4067, https://doi.org/10.1039/d1ta09516a.

[23] R. Pan, Z. Wang, R. Sun, J. Lindh, K. Edström, M. Strømme, L. Nyholm, Thickness difference induced pore structure variations in cellulosic separators for lithium-ion batteries, Cellulose 24 (2017) 2903–2911, https://doi.org/10.1007/s10570-017-1312-z.

[24] R. Gonçalves, E. Lizundia, M.M. Silva, C.M. Costa, S. Lanceros-Méndez, Mesoporous cellulose nanocrystal membranes as battery separators for environmentally safer lithium-ion batteries, ACS Appl. Energy Mater. 2 (2019) 3749–3761, https://doi.org/10.1021/acsaem.9b00458.

[25] E.R.P. Keijsers, G. Yilmaz, J.E.G. Van Dam, The cellulose resource matrix, Carbohydr. Polym. 93 (2013) 9–21, https://doi.org/10.1016/j.carbpol.2012.08.110.

[26] TAPPI standards. regulations and style guidelines, WI 3021, 2013.

[27] R. D'Orsi, V.C. Canale, R. Cancelliere, O.H. Omar, C. Mazzuca, L. Micheli, A. Operamolla, Tailoring the chemical structure of cellulose nanocrystals by amine functionalization, Eur. J. Org. Chem. 26 (2023) e202201457, https://doi.org/10.1002/ejoc.202201457.

[28] N. Lin, A. Dufresne, Surface chemistry, morphological analysis and properties of cellulose nanocrystals with gradiented sulfation degrees, Nanoscale 6 (2014) 5384–5393, https://doi.org/10.1039/C3NR06761K.

[29] L. Spagnuolo, D. Beneventi, A. Dufresne, A. Operamolla, High yield synthesis of cellulose nanocrystals from Avicel by mechano-enzymatic approach, ChemistrySelect 9 (2024) e202401511, https://doi.org/10.1002/slct.202401511.

[30] N. Lin, A. Dufresne, Nanocellulose in biomedicine: current status and future prospect, Eur. Polym. J. 59 (2014) 302–325, https://doi.org/10.1016/j.eurpolymj.2014.07.025.

[31] M. Skočaj, Bacterial nanocellulose in papermaking, Cellulose 26 (2019) 6477–6488, https://doi.org/10.1007/s10570-019-02566-y.

[32] W. Chen, H. Yu, S.-Y. Lee, T. Wei, J. Li, Z. Fan, Nanocellulose: a promising nanomaterial for advanced electrochemical energy storage, Chem. Soc. Rev. 47 (2018) 2837–2872, https://doi.org/10.1039/C7CS00790F.

[33] A.H. Tayeb, E. Amini, S. Ghasemi, M. Tajvidi, Cellulose nanomaterials-binding properties and applications: a review, Molecules 23 (2018) 2684, https://doi.org/10.3390/molecules23102684.

[34] D.J. Gardner, G.S. Oporto, R. Mills, M.A.S.A. Samir, Adhesion and surface issues in cellulose and nanocellulose, J. Adhes. Sci. Technol. 22 (2008) 545–567, https://doi.org/10.1163/156856108X295509.

[35] M.A. Hubbe, O.J. Rojas, L.A. Lucia, Green modification of surface characteristics of cellulosic materials at the molecular or nano scale: a review, BioRosources 10 (2015) 6095–6206, https://doi.org/10.15376/biores.10.3.Hubbe.

[36] S.H. Osong, S. Norgren, P. Engstrand, Processing of wood-based microfibrillated cellulose and nanofibrillated cellulose, and applications relating to papermaking: a review, Cellulose 23 (2016) 93–123, https://doi.org/10.1007/s10570-015-0798-5.

[37] S. Trano, D. Versaci, M. Castellino, M. Fontana, L. Fagiolari, C. Francia, F. Bella, Exploring nature-behaviour relationship of carbon black materials for potassium-ion battery electrodes, Energy Mater 4 (2024) 400008, https://doi.org/10.20517/energymater.2023.79.

[38] A. Operamolla, S. Casalini, D. Console, L. Capodieci, F. Di Benedetto, G.V. Bianco, G. V, F. Babudri, Tailoring water stability of cellulose nanopaper by surface functionalization, Soft Matter 14 (2018) 7390–7400, https://doi.org/10.1039/C8SM00433A.

[39] A. Operamolla, C. Mazzuca, L. Capodieci, F. Di Benedetto, L. Severini, M. Titubante, A. Martinelli, V. Castelvetro, L. Micheli, Toward a reversible consolidation of paper materials using cellulose nanocrystals, ACS Appl. Mater. Interfaces 13 (2021) 44972–44982, https://doi.org/10.1021/acsami.1c15330.

[40] M.E. Spahr, D. Goers, A. Leone, S. Stallone, E. Grivei, Development of carbon conductive additives for advanced lithium ion batteries, J. Power Sources 196 (2011) 3404–3413, https://doi.org/10.1016/j.jpowsour.2010.07.002.

[41] J.H. Park, S.H. Kim, K.H. Ahn, Role of carboxymethyl cellulose binder and its effect on the preparation process of anode slurries for Li-ion batteries, Colloids Surf., A 664 (2023) 131130, https://doi.org/10.1016/j.colsurfa.2023.131130.

[42] X. Wu, Y. Chen, Z. Xing, C.W.K. Lam, S.S. Pang, W. Zhang, Z. Ju, Advanced carbon-based anodes for potassium-ion batteries, Adv. Energy Mater. 9 (2019) 1900343, https://doi.org/10.1002/aenm.201900343.

[43] H. Wang, D. Zhai, F. Kang, Solid electrolyte interphase (SEI) in potassium ion batteries, Energy Environ. Sci. 13 (2020) 4583–4608, https://doi.org/10.1039/d0ee01638a.

[44] T.S. Mathis, N. Kurra, X. Wang, D. Pinto, P. Simon, Y. Gogotsi, Energy storage data reporting in perspective—Guidelines for interpreting the performance of electrochemical energy storage systems, Adv. Energy Mater. 9 (2019) 1902007, https://doi.org/10.1002/aenm.201902007.

[45] W. Zhou, B. He, L. Quan, R. Li, Y. Chen, C. Fan, S. Chen, C. Xu, X. Fan, L. Zing, J. Liu, Binder chemistry dependent electrolyte reduction in potassium-ion

batteries: a successive, two-step reduction way, Adv. Energy Mater. 13 (2023) 2202874, https://doi.org/10.1002/aenm.202202874.
[46] L. Yan, Q. Ren, J. Wang, L. Fan, X. Mei, W. Lei, Z. Shi, Integrated design from microstructural engineering to binder optimization enabling a practical carbon anode with ultrahigh ICE and efficient potassium storage, ACS Appl. Mater. Interfaces 14 (2022) 48715–48726, https://doi.org/10.1021/acsami.2c13970.
[47] J. Li, N. Zhuang, J. Xie, Y. Zhu, H. Lai, W. Qin, M.S. Javed, W. Xie, W. Mai, Carboxymethyl cellulose binder greatly stabilizes porous hollow carbon submicrospheres in capacitive K-ion storage, ACS Appl. Mater. Interfaces 11 (2019) 15581–15590, https://doi.org/10.1021/acsami.9b02060.
[48] Z. Li, W. Shin, Y. Chen, J.C. Neuefeind, P.A. Greaney, X. Ji, Low temperature pyrolyzed soft carbon as high capacity K-ion anode, ACS Appl. Energy Mater. 2 (2019) 4053–4058, https://doi.org/10.1021/acsaem.9b00125.
[49] E.J. Kim, P.R. Kumar, Z.T. Gossage, K. Kubota, T. Hosaka, R. Tatara, S. Komaba, Active material and interphase structures governing performance in sodium and potassium ion batteries, Chem. Sci. 13 (2022) 6121–6158, https://doi.org/10.1039/D2SC00946C.
[50] Z.T. Gossage, D. Igarashi, Y. Fujii, M. Kawaguchi, R. Tatara, K. Nakamoto, S. Komaba, New frontiers in alkali metal insertion into carbon electrodes for energy storage, Chem. Sci. 15 (2024) 18272–18294, https://doi.org/10.1039/D4SC03203A.
[51] Z. Wu, J. Zou, S. Shabanian, K. Golovin, J. Liu, The roles of electrolyte chemistry in hard carbon anode for potassium-ion batteries, Chem. Eng. J. 427 (2022) 130972, https://doi.org/10.1016/j.cej.2021.130972.
[52] S. Sawalha, F. Milano, M.R. Guascito, S. Bettini, L. Giotta, A. Operamolla, T. Da Ros, M. Prato, L. Valli, Improving 2D-organization of fullerene Langmuir-Schäfer thin films by interaction with cellulose nanocrystals, Carbon N Y 167 (2020) 906–917, https://doi.org/10.1016/j.carbon.2020.05.084.
[53] A. Hajian, S.B. Lindström, T. Pettersson, M.M. Hamedi, L. Wågberg, Understanding the dispersive action of nanocellulose for carbon nanomaterials, Nano Lett. 17 (2017) 1439–1447, https://doi.org/10.1021/acs.nanolett.6b04405.
[54] B. Cao, Q. Zhang, H. Liu, B. Xu, S. Zhang, T. Zhou, J. Mao, W.K. Pang, Z. Guo, A. Li, J. Zhou, X. Chen, H. Song, Graphitic carbon nanocage as a stable and high power anode for potassium-ion batteries, Adv. Energy Mater. 8 (2018) 1801149, https://doi.org/10.1002/aenm.201801149.
[55] J.Y. Song, H.H. Lee, Y.Y. Wang, C.C. Wan, Two-and three-electrode impedance spectroscopy of lithium-ion batteries, J. *Power Sources* 111 (2002) 255–267, https://doi.org/10.1016/S0378-7753(02)00310-5.